Comparison of two- and three-layer restacked Dion–Jacobson phase niobate nanosheets as catalysts for photochemical hydrogen evolution†

Kazuhiko Maeda‡ and Thomas E. Mallouk*

Received 23rd February 2009, Accepted 16th April 2009
First published as an Advance Article on the web 28th May 2009
DOI: 10.1039/b903692j

Restacked niobate nanosheets were prepared by exfoliation of the corresponding Dion–Jacobson type layered perovskites ($HCa_2Nb_3O_{10}$, $HSr_2Nb_3O_{10}$ and $HLaNb_2O_7$) with tetra(*n*-butyl)ammonium hydroxide and subsequent treatment with hydrochloric acid. The nanosheets were characterized by means of X-ray diffraction, scanning electron microscopy, Raman spectroscopy, and diffuse reflectance spectroscopy. With modification by platinum nanoparticles as additional catalysts, these nanosheet materials were tested as photocatalysts for hydrogen evolution from water containing 2-propanol as an electron donor under ultraviolet irradiation ($\lambda > 300$ nm). The activity of a triple-layered nanosheet ($HSr_2Nb_3O_{10}$) was an order of magnitude higher than that of the $HLaNb_2O_7$ nanosheet with double perovskite layers, despite their physicochemical similarity. Physicochemical analyses suggested that in triple-layered perovskite nanosheets, photocatalytic activity is influenced by several factors including the conduction band potential and the band-gap energy (the number of available photons), which are derived from the distortion of perovskite blocks consisting of NbO_6 octahedra.

Introduction

Dion–Jacobson phase layered perovskite oxides and their derivatives exhibit a range of interesting properties including ion-exchange,[1] intercalation,[2] electronic/protonic-conductivity,[3] superconductivity,[4] dielectric behavior,[5] photoluminescence,[6] and photocatalytic properties.[7–14] Layered niobates, expressed as $AB_2Nb_3O_{10}$ and $ALaNb_2O_7$ (A = H, K, Rb, Cs; B = Ca, Sr) for three- and two-layer compounds, respectively, were originally developed by Domen *et al.* as semiconductor photocatalysts for water splitting.[7] These compounds consist of negatively charged perovskite sheets that stack to form a two-dimensional layered structure interleaved with A^+ cations for compensation of the negative charge of sheets.[15] Upon photoexcitation, electrons and holes are generated in the sheets, causing redox reactions with reactant molecules adjacent to the layers. Therefore, the primary requirement to achieve high efficiency using a layered photocatalyst is the intercalation of reactant molecules (*e.g.*, H_2O) into the interlayer galleries, because of enhanced access of photogenerated carriers to reactants.[7–9]

One of the most convenient ways to utilize the interlayer nanospace for reactions is a technique called "exfoliation–restacking".[10,13] Certain layered metal oxides can be exfoliated by reaction with bulky base molecules, yielding unilamellar nanosheet colloids.[2,10,12,13] The colloidal nanosheets are readily restacked by changing the ionic strength or pH of the colloidal suspension to give aggregates of nanosheets that have much higher specific surface area than the parent layered material.[10] The colloidal nanosheets and the restacked aggregates are attractive building blocks for self-assembled nanostructures[6b] and artificial photosynthetic assemblies that incorporate catalytic nanoparticles[12,13] or light-harvesting metal complexes.[16] For applications in photocatalytic water splitting, our group has recently reported on the modification of the interlayer galleries of restacked $KCa_2Nb_3O_{10}$ nanosheets with highly dispersed rhodium oxide (Rh_2O_3) nanoparticles. These materials efficiently catalyze H_2 evolution from aqueous methanol solution under ultraviolet (UV) irradiation ($\lambda > 300$ nm).[13] The loaded Rh_2O_3 nanoparticles collect photogenerated electrons from the photoactive $Ca_2Nb_3O_{10}^-$ layers and provide catalytic sites for H_2 evolution, resulting in a higher rate of H_2 evolution than that found with analogous platinum-loaded materials. To further enhance the photocatalytic activity, however, it is important not only to develop such nanoparticle catalysts but also to understand the characteristics of the nanosheets as low-dimensional semiconductors.[17]

In general, the functionality (including photocatalytic properties) of a given material is strongly dependent on its structure. Therefore, investigating the relationship between the functionality and structure of a material is of interest and expected to provide useful information. While the relationship between the structural characteristics and the photocatalytic performance of some Dion–Jacobson type layered perovskites has been examined,[11] there is little information about structural effects in the case of nanosheets. Since photoexcitation of perovskite nanosheets occurs in the two-dimensional perovskite blocks that are generally well hydrated, the photocatalytic activity is expected to be a stronger function of the intrinsic properties of the nanosheet, more than in the case of the layered parent compounds, in which the degree of hydration of the interlayer galleries is also a key parameter.

Department of Chemistry, The Pennsylvania State University, University Park, Pennsylvania, 16802, USA. E-mail: tom@chem.psu.edu; Fax: +1 814 863 8403; Tel: +1 814 863 9637

† Electronic supplementary information (ESI) available: Comparison of H_2 evolution activity of restacked $HCa_2Nb_3O_{10}$ nanosheets with that of P25 titania. See DOI: 10.1039/b903692j.

‡ Research fellow of the Japan Society of Promotion Science (JSPS).

This paper reports structural effects in photocatalytic H_2 evolution from three different kinds of nanosheets derived from $HCa_2Nb_3O_{10}$, $HSr_2Nb_3O_{10}$ and $HLaNb_2O_7$. Photocatalytic activity is examined for UV photolysis from aqueous 2-propanol solution under band-gap irradiation ($\lambda > 300$ nm). Factors affecting the activity are discussed on the basis of structural analyses.

Experimental

Preparation of restacked Dion–Jacobson type layered perovskite niobate nanosheets

Layered $KCa_2Nb_3O_{10}$, $KSr_2Nb_3O_{10}$ and $RbLaNb_2O_7$ powders were prepared by the conventional solid state route according to the previous literature reports.[1a,3c] Proton exchange was carried out in aqueous nitric acid (4 M) at room temperature for at least 3 days with daily centrifugation and replacement of the acid solution. The product was isolated by centrifugation, washing, and finally drying in an oven at 333 K overnight.

Exfoliation of the as-prepared proton-exchanged materials was performed using aqueous tetra(*n*-butyl)ammonium hydroxide (TBA^+OH^-, Aldrich, 40 wt% in H_2O) at room temperature in a similar manner to that reported by Ebina *et al.*[10] The powder was shaken in aqueous solution containing an appropriate amount of TBA^+OH^- for 1 week. The molar ratio of TBA^+OH^- to the exchangeable cations in the lamellar solids was 1.0. After removing unreacted solids, the resulting nanosheet colloids were restacked by adding aqueous hydrochloric acid (HCl, 2.5 M) to form precipitates. This solid was then rinsed several times with pure water to remove residual TBA^+Cl^- and HCl, followed by drying in an oven at 333 K overnight and grinding into a powder using a mortar and pestle. Energy dispersive X-ray (EDX) spectroscopy revealed that the acid-precipitated colloids contained little residual potassium or rubidium, with K/Nb (Rb/Nb) ratios of 0.01–0.03. The final products are thus represented below as restacked nanosheets of $HCa_2Nb_3O_{10}$, $HSr_2Nb_3O_{10}$ and $HLaNb_2O_7$.

Modification with platinum nanoparticles

Nanoparticles of platinum (Pt) as a catalyst for H_2 evolution were loaded by an *in situ* photodeposition method[18] onto the external surface of the as-prepared nanosheet materials following the procedure described in our previous paper.[16] The anionic platinum complex H_2PtCl_6 was used as the precursor. The loading of Pt was 0.3 wt%.

Characterization of materials

Powder X-ray diffraction (XRD) patterns were obtained with a Philips X'Pert MPD diffractometer using Cu Kα radiation, and scanning electron micrographs (SEMs) were obtained using a Hitachi S-4700 microscope. The Brunauer, Emmett, Teller (BET) surface area was measured using a Micromeritics ASAP 2010 instrument at liquid nitrogen temperature. Before nitrogen adsorption isotherms were acquired, the samples were evacuated at 353–363 K for at least 24 h. Raman spectra were obtained with a Jasco NRS-3100 spectrometer. UV-visible diffuse reflectance spectra were recorded using a Jasco V-560 spectrometer equipped with an integrating sphere. A $BaSO_4$ plate was used as the reference to correct the spectra. The spectra were converted from reflectance to absorption by the following equation:

$$\text{Absorption (\%)} = 100 - r \quad (1)$$

where r indicates the percent relative reflectance.

UV photolysis from aqueous 2-propanol solution

The reaction was performed by dispersing 5.0 mg of the Pt-loaded sample containing 1 M 2-propanol as an electron donor using a Pyrex reaction cell (10 mL capacity) sealed with a rubber septum. To eliminate the complication of intercalation effects, 2-propanol was employed because it has less accessibility to the interlayer galleries of perovskite niobates.[7,9] The reactant solution was purged with argon for 5–10 min to remove dissolved air, and was then placed in an outer glass jacket where argon gas flowed continuously, to prevent air contamination during the reaction. After that, the reaction vessel was irradiated with a 300 W xenon lamp ($\lambda > 300$ nm). The evolved gases were analyzed by gas chromatography with a thermal conductivity detector and molecular sieve 5A columns at ambient temperature.

Results and discussion

Structural properties

Fig. 1 shows the XRD patterns of the restacked $HCa_2Nb_3O_{10}$, $HSr_2Nb_3O_{10}$ and $HLaNb_2O_7$ nanosheets, along with reference patterns of the corresponding lamellar materials. In all cases, the XRD patterns of the restacked samples give a very weak (001) diffraction peak and a complete absence of (00l) ($l \geq 2$) peaks, indicating that the periodic layered structure of the original materials almost disappears upon exfoliation with TBA^+OH^- and subsequent restacking process. However, (100) and (110) diffraction peaks corresponding to in-plane diffraction are preserved in the XRD patterns. This result indicates that the two-dimensional structure of perovskite sheets is preserved after the exfoliation–restacking procedure in all cases. The position of the

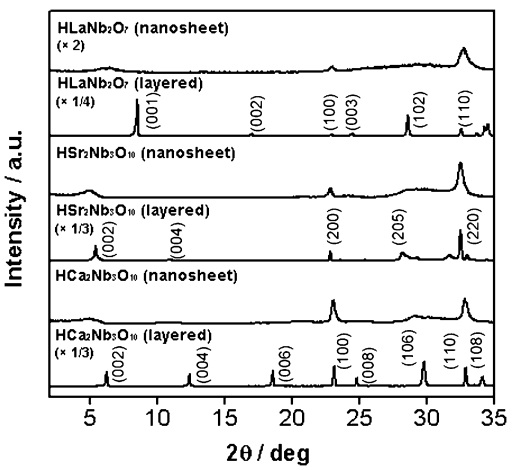

Fig. 1 XRD patterns of restacked nanosheets of $HCa_2Nb_3O_{10}$, $HSr_2Nb_3O_{10}$ and $HLaNb_2O_7$, along with data for the corresponding layered materials.

(001) diffraction peak in all restacked nanosheets appears at lower 2θ angles than that in the corresponding layered materials, indicating more hydration of the nanosheet materials. These results are consistent with the previous studies.[3c,19]

SEM images of the same samples are shown in Fig. 2. After exfoliation of lamellar $HCa_2Nb_3O_{10}$ and subsequent reassembly by HCl, the original layered structure was completely destroyed, producing aggregated solids with a disordered structure. This is consistent with the XRD result (Fig. 1). There is no distinct difference in surface morphology among the three nanosheet samples. The specific surface areas were 50–51 $m^2\ g^{-1}$ for $HCa_2Nb_3O_{10}$, 56–57 $m^2\ g^{-1}$ for $HSr_2Nb_3O_{10}$ and 68–69 $m^2\ g^{-1}$ for $HLaNb_2O_7$. By comparison, the surface areas of the parent solids are typically in the range of 1 $m^2\ g^{-1}$.

Raman spectroscopy was employed to obtain information on the local structure of the restacked $HCa_2Nb_3O_{10}$, $HSr_2Nb_3O_{10}$ and $HLaNb_2O_7$ nanosheets. Fig. 3 shows the Raman spectra for $HCa_2Nb_3O_{10}$ before and after the exfoliation–restacking process, respectively. The assignment of the Raman bands is possible according to previous studies on the corresponding layered materials.[20] Layered $HCa_2Nb_3O_{10}$ gives Raman bands at

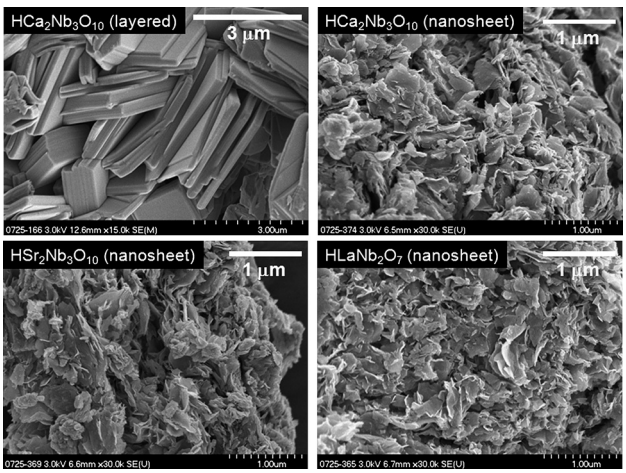

Fig. 2 SEM images of layered $HCa_2Nb_3O_{10}$, and restacked nanosheets of $HCa_2Nb_3O_{10}$, $HSr_2Nb_3O_{10}$, and $HLaNb_2O_7$.

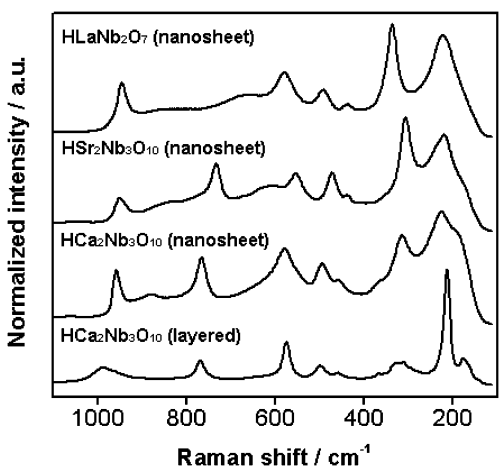

Fig. 3 Raman spectra for layered $HCa_2Nb_3O_{10}$, and restacked nanosheets of $HCa_2Nb_3O_{10}$, $HSr_2Nb_3O_{10}$, and $HLaNb_2O_7$.

around 990, 770, 575, 495, 460, and 400–100 cm^{-1}. However, Raman bands for the restacked $HCa_2Nb_3O_{10}$ nanosheet became broader than those for the original layered material, while maintaining the positions except for a 990 cm^{-1} band that is assigned to a vibrational mode of the Nb–O terminal bond. This indicates that the local structure of $HCa_2Nb_3O_{10}$ remains almost unchanged even after the exfoliation–restacking process. The red shift and sharpening of the 990 cm^{-1} band after exfoliation–restacking can be explained by the fact that the restacked material is more hydrated than the parent solid, as has been reported by Jehng and Wachs who performed an *in situ* Raman study on $HCa_2Nb_3O_{10}$.[20a] More hydration of the $HCa_2Nb_3O_{10}$ nanosheet also results in the appearance of an additional Raman band at 880 cm^{-1}. This is assignable to an anti-symmetric stretching mode of Nb–O bond, and is better resolved in the hydrated state.[20a] The results of the present Raman study on $HCa_2Nb_3O_{10}$ materials are in good agreement with those of XRD and SEM analyses (Fig. 1 and 2).

For the restacked $HCa_2Nb_3O_{10}$, $HSr_2Nb_3O_{10}$ and $HLaNb_2O_7$ nanosheets, all spectra are broad due primarily to less structural periodicity, as mentioned earlier. The spectral shapes of $HCa_2Nb_3O_{10}$ and $HSr_2Nb_3O_{10}$ are similar to each other, indicating that the two materials have similar local structure. However, the positions of the Raman bands in $HSr_2Nb_3O_{10}$ are shifted to lower wavenumbers than those in $HCa_2Nb_3O_{10}$. A longer bond distance, in principle, results in a shift of Raman bands to lower wavenumbers. Although the detailed crystal structure of $HSr_2Nb_3O_{10}$ (or $KSr_2Nb_3O_{10}$) has yet to be reported, it is most likely that substitution of Ca^{2+} cations (ionic radius 1.48 Å in 12 coordination) for the larger Sr^{2+} ions (1.58 Å)[21] expands the perovskite layers and relaxes the lattice distortion, resulting in the overall red shift. An identical red shift has been reported in lamellar $CsB_2Nb_3O_{10}$ (B = Ca, Sr, and Ba) where the perovskite layers expand in the order of Ca < Sr < Ba.[20b] The spectral shape of the $HLaNb_2O_7$ nanosheet may seem somewhat similar to those of $HCa_2Nb_3O_{10}$ and $HSr_2Nb_3O_{10}$, but it differs in that the band at 800–700 cm^{-1}, derived from central NbO_6 octahedra in the triple perovskite blocks,[20b] is absent. The difference can be attributed to the fact that $HLaNb_2O_7$ has double perovskite layers, whereas $HCa_2Nb_3O_{10}$ and $HSr_2Nb_3O_{10}$ consist of triple layers.[1a–c,15] Thus, Raman spectroscopy can clearly distinguish the local structure of the restacked nanosheet materials, which is difficult to resolve by XRD analysis.

Light-absorption properties and band structures

UV-visible absorption spectra for the same samples are shown in Fig. 4. All samples exhibit absorption bands in the UV region (<400 nm). The position of the absorption edge moves to longer wavelengths in the order of $HCa_2Nb_3O_{10}$ < $HSr_2Nb_3O_{10}$ < $HLaNb_2O_7$. The band-gap energies of the materials were estimated using the following equation:[22]

$$\alpha h\nu = (h\nu - E_g)^n \quad (2)$$

where α, E_g, and n are, respectively, the absorption coefficient (Kubelka–Munk function), band gap, and an exponent that is 2 for indirect-gap semiconductors and ½ for direct-gap

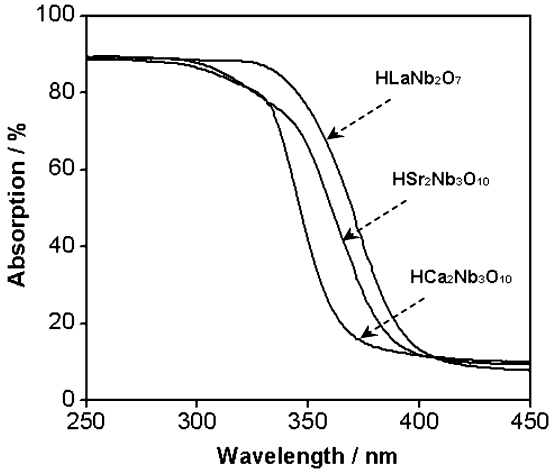

Fig. 4 UV-visible absorption spectra for restacked nanosheets of $HCa_2Nb_3O_{10}$, $HSr_2Nb_3O_{10}$ and $HLaNb_2O_7$.

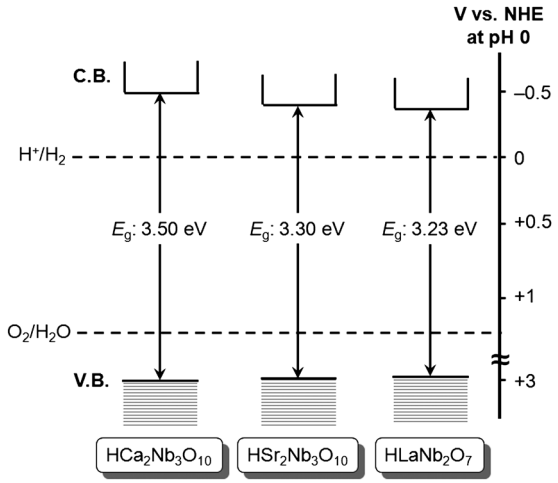

Fig. 5 A schematic illustration of band structures of restacked nanosheets of $HCa_2Nb_3O_{10}$, $HSr_2Nb_3O_{10}$ and $HLaNb_2O_7$.

semiconductors.[23] From the plot of $(\alpha h\nu)^{1/n}$ *vs.* $h\nu$, the band gap (E_g) can be obtained by extrapolating the linear portion to the $h\nu$ axis intercept. Assuming that the materials are indirect band-gap semiconductors ($n = 2$), one can estimate the band-gap energies of the restacked nanosheets of $HCa_2Nb_3O_{10}$, $HSr_2Nb_3O_{10}$ and $HLaNb_2O_7$ to be 3.50, 3.30 and 3.23 eV, respectively.

The band-gap energy of layered perovskite materials consisting of NbO_6 octahedral units is affected by several factors including the distortion of NbO_6 units, the thickness of perovskite layers, and the electronegativity of elements on the octahedral and 12-coordinate sites.[24] In the present case, it appears that the distortion of NbO_6 units in the perovskite layers is the main factor determining the band-gap energies. Blasse *et al.* have reported the relationship between crystal structures and energy delocalization for $ANbO_3$ (A = Li, Na, and K) with a distorted perovskite structure consisting of corner-sharing NbO_6 octahedral units.[25] According to that study, the relatively weak interaction between NbO_6 octahedra in $LiNbO_3$ results in localization of the excited state energy, because a bond angle of Nb–O–Nb is far from the ideal angle of 180° (most favorable for π-bonding), *i.e.*, the NbO_6 octahedral units are tilted. On the other hand, the excited state energy is delocalized in $NaNbO_3$ and $KNbO_3$ in which the bond angles are closer to 180°. The delocalization of excited state energy causes the position of absorption band edge to be shifted to longer wavelength, due to broadening of the energy band. Accordingly, the band-gap energy of $ANbO_3$ decreases from $LiNbO_3$ to $KNbO_3$. As revealed by Raman spectroscopy (Fig. 3), the distortion of NbO_6 octahedra in the perovskite blocks of $HSr_2Nb_3O_{10}$ is more relaxed than in $HCa_2Nb_3O_{10}$, thereby resulting in greater delocalization of the excited state energy and decreasing band-gap energy. The smaller band gaps of Sr materials relative to their Ca analogues have been also reported for other perovskite niobates.[7a,24] The smallest band gap of the $HLaNb_2O_7$ nanosheet among the materials examined could also be explained in terms of the minimal tilting of the constituent NbO_6 units. As reported previously, the corner-sharing NbO_6 octahedra in the perovskite layers of $HLaNb_2O_7$ are connected with a tilt angle close to 180°,[1c] whereas the tilt angle in $HCa_2Nb_3O_{10}$ is obviously smaller than 180°.[15] This difference in the tilt angle accounts for the order of band-gap energies, although quantitative comparisons are difficult because of the lack of detailed information about the crystal structure of $HSr_2Nb_3O_{10}$ (or $KSr_2Nb_3O_{10}$).

The conduction band edge potential of a semiconductor is one of the important parameters affecting the overall efficiency of H_2 production from water. The conduction band edge should lie at a potential more negative than the water reduction potential (<0 V *vs.* NHE at pH 0). Matsumoto has noted an empirical correlation between the conduction band potential (E_{CB}) of metal-oxide semiconductors containing d^0 and d^{10} metal ions and the band gaps (E_g) as follows:[26]

$$E_{CB} \approx 1.23 - E_g/2 \quad (3)$$

Thus, we can estimate the conduction band potentials of restacked $HCa_2Nb_3O_{10}$, $HSr_2Nb_3O_{10}$ and $HLaNb_2O_7$ nanosheets from their band-gap energies. The band structures of these nanosheets are schematically illustrated in Fig. 5. The potential of the conduction band edge becomes more negative from $HLaNb_2O_7$ to $HCa_2Nb_3O_{10}$, suggesting that the driving force for water reduction by electrons in the conduction band of $HCa_2Nb_3O_{10}$ is larger than that of the $HSr_2Nb_3O_{10}$ and $HLaNb_2O_7$ nanosheets.

Photocatalytic activity

Fig. 6 shows the time courses of H_2 production from aqueous 2-propanol solutions using Pt-loaded restacked nanosheets of $HCa_2Nb_3O_{10}$, $HSr_2Nb_3O_{10}$ and $HLaNb_2O_7$ under UV irradiation ($\lambda > 300$ nm). In these reactions, both the photoreduction of H^+ to H_2 and the photooxidation of 2-propanol occur mainly on the external surface of the restacked nanosheets, because Pt nanoparticles that function as H_2 evolution catalysts are loaded there, and 2-propanol has little accessibility to the interlayer galleries of the restacked nanosheets.[7,9,14] All materials exhibited reasonable activity, and the amount of H_2 produced increased linearly with reaction time. This is consistent with the idea that the conduction band edges of these materials are located at

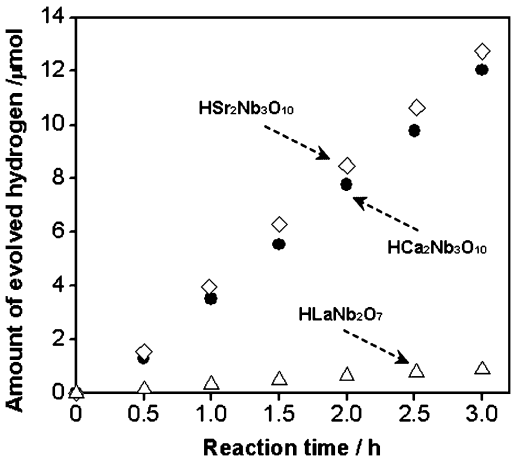

Fig. 6 Time courses of H_2 evolution from Pt-loaded restacked nanosheets of $HCa_2Nb_3O_{10}$, $HSr_2Nb_3O_{10}$ and $HLaNb_2O_7$ under UV irradiation ($\lambda > 300$ nm). Reaction conditions: catalyst, 5.0 mg; aqueous 2-propanol solution (1 M, 2.0 mL); light source, xenon lamp (300 W).

potentials that are negative of the H^+/H_2 couple (0 V *vs.* NHE at pH 0), as illustrated in Fig. 5. The sequence of the activity was $HCa_2Nb_3O_{10} \approx HSr_2Nb_3O_{10} \gg HLaNb_2O_7$. No gas evolution was observed in the dark.

The fact that the activity of the $HLaNb_2O_7$ nanosheets was an order of magnitude lower than those of the $HCa_2Nb_3O_{10}$ and $HSr_2Nb_3O_{10}$ appears peculiar, since the physicochemical properties of the $HLaNb_2O_7$ nanosheets are similar to those of $HSr_2Nb_3O_{10}$, as listed in Table 1. The principal structural difference between the two materials is the number of perovskite blocks. As mentioned above, $HSr_2Nb_3O_{10}$ is a three-layer perovskite, whereas $HLaNb_2O_7$ is two-layered. One possible explanation is the difference in reactivity of charge carriers at the nanosheet surface. Machida *et al.* conducted computational studies on $RbLaTa_2O_7$ (two-layer perovskite) and $RbCa_2Ta_3O_{10}$ (three-layer perovskite) to predict the difference in photocatalytic activity for overall water splitting between two materials.[11a,b] Their study suggests that the reactivity of holes in the valence band (populated by oxygen 2p orbitals) with intercalated molecules varies with respect to the number of perovskite layers, and that the terminal oxygen atoms facing the interlayer galleries in the three-layer perovskite make a strong contribution to the formation of the valence band maximum, whereas those in the two-layer perovskite do not. As a result, the three-layer perovskite exhibits higher reactivity than the two-layer analogue. In the present case, therefore, the low activity of the restacked $HLaNb_2O_7$ nanosheet (two-layer perovskite) might be explained in terms of the low reactivity of photogenerated holes in the valence band as well.

Table 1 Physicochemical properties and photocatalytic activities of $HCa_2Nb_3O_{10}$, $HSr_2Nb_3O_{10}$ and $HLaNb_2O_7$ nanosheets

Nanosheet material	Specific surface area/m^2 g^{-1}	Band-gap energy[a]/eV	Conduction band potential[b]/V *vs.* NHE at pH 0	Steady rate of H_2 evolution[c]/μmol h^{-1}
$HCa_2Nb_3O_{10}$	50–51	3.50	−0.52	4.2
$HSr_2Nb_3O_{10}$	56–57	3.30	−0.42	4.5
$HLaNb_2O_7$	68–69	3.23	−0.39	0.3

[a] Estimated using eqn (2) (see text). [b] Estimated using eqn (3) (see text). [c] Reaction conditions: catalyst, 5.0 mg (0.3 wt% Pt-loaded); reaction solution, aqueous solution containing 1 M 2-propanol (2.0 mL); irradiation wavelength, $\lambda > 300$ nm.

Among three-layer perovskite nanosheets, the activity of $HSr_2Nb_3O_{10}$ is comparable or slightly higher than that of $HCa_2Nb_3O_{10}$. In isostructural compounds such as solid solutions, it is known that the photocatalytic activity for H_2 evolution from water containing sacrificial electron donors generally increases with the conduction band edge potential.[27–29] Nevertheless, the $HSr_2Nb_3O_{10}$ nanosheet having a more positive conduction band edge potential exhibits a similar level of activity to $HCa_2Nb_3O_{10}$. Presumably, the wider absorption band of the $HSr_2Nb_3O_{10}$ nanosheet makes up for its slightly more positive conduction band edge potential in determining the overall yield of H_2 evolution. This idea is consistent with the previous report on $Ga_{2-x}In_xO_3$ solid solutions as photocatalysts for H_2 evolution from aqueous methanol solutions under UV irradiation ($\lambda >$ 300 nm). In that case, the activity of $Ga_{2-x}In_xO_3$ is increased up to $x = 1$ with a shift of the absorption edge to longer wavelengths, as the position of the conduction band edge becomes more positive.[30] Another possibility is the distortion of NbO_6 octahedra in the perovskite layers. As mentioned earlier, the distortion of perovskite layers is greater in $HCa_2Nb_3O_{10}$ than in $HSr_2Nb_3O_{10}$ owing to the lattice expansion, implying that the photogenerated electron–hole pairs in the perovskite blocks of $HSr_2Nb_3O_{10}$ can migrate more smoothly than those in $HCa_2Nb_3O_{10}$. The mobility of charge carriers should affect the photocatalytic activity as well as the conduction band potential and the band-gap energy, because it affects the probability that charge carriers reach reaction sites on the surface.[31] It is thus possible that the distortion of NbO_6 octahedra in the perovskite blocks affects the charge separation and/or charge transport process, resulting in different photocatalytic activities.

For benchmarking purposes, it is useful to compare the photoactivity of these materials with other widely tested photocatalysts. Comparisons with P25 titania (see ESI†) showed that the activity of restacked $HCa_2Nb_3O_{10}$ nanosheet under UV photolysis is two times lower than that of P25 in aqueous methanol solution (Fig. S1†). On the other hand, the nanosheets exhibit substantially higher photocatalytic activity for H_2 evolution when sensitized by tris(2,2′-bipyridyl)ruthenium(II) chloride with visible light, compared to P25 (Fig. S2†). Nevertheless, it should be stressed that the optimal conditions (*e.g.*, Pt-loading) for a given reaction system usually vary with the photocatalytic material used.[10a]

Conclusions

Using three different restacked perovskite nanosheets ($HCa_2Nb_3O_{10}$, $HSr_2Nb_3O_{10}$ and $HLaNb_2O_7$) as photocatalysts, the photocatalytic activity for H_2 production in UV photolysis from 2-propanol solution was examined. Even though there is little difference in the physicochemical characteristics of $HSr_2Nb_3O_{10}$ and $HLaNb_2O_7$ nanosheets, the photocatalytic activity of the former is an order of magnitude higher than that of the latter. In three-layer perovskite nanosheets, the tilting of NbO_6 octahedra in the perovskite layers affects properties such as the conduction band

edge potential and the band-gap energy, which affect the overall photocatalytic activity in a complex manner.

Acknowledgements

The authors thank Prof. Kazunari Domen (Department of Chemical System Engineering, The University of Tokyo) for SEM/EDX and UV-visible measurements. For assistance in Raman spectroscopy, we thank Prof. Michikazu Hara and Dr Kiyotaka Nakajima (Materials and Structures Laboratory, Tokyo Institute of Technology). This work was supported by the Office of Basic Energy Sciences, Division of Chemical Sciences, Geosciences, and Energy Biosciences, Department of Energy under contract DE-FG02-07ER15911. K.M. gratefully acknowledges the support of a Japan Society for the Promotion of Science (JSPS) Fellowship.

References

1 (*a*) M. Dion, M. Ganne and M. Tournoux, *Mater. Res. Bull.*, 1981, **16**, 1429; (*b*) A. J. Jacobson, J. W. Johnson and J. T. Lewandowski, *Inorg. Chem.*, 1985, **24**, 3727; (*c*) J. Gopalakrishnan, V. Bhat and B. Raveau, *Mater. Res. Bull.*, 1987, **22**, 413; (*d*) S. Uma, A. R. Raju and J. Gopalakrishnan, *J. Mater. Chem.*, 1993, **3**, 709; (*e*) K. Toda, T. Teranishi, Z.-G. Ye, M. Sato and Y. Hinatsu, *Mater. Res. Bull.*, 1999, **34**, 971.

2 (*a*) M. M. J. Treacy, S. B. Rice, A. J. Jacobson and J. T. Lewandowski, *Chem. Mater.*, 1990, **2**, 279; (*b*) Y.-S. Han, I. Park and J.-H. Choy, *J. Mater. Chem.*, 2001, **11**, 1277; (*c*) H. Hata, S. Kubo, Y. Kobayashi and T. E. Mallouk, *J. Am. Chem. Soc.*, 2007, **129**, 3064.

3 (*a*) V. Thangadurai, P. Schmid-Beurmann and W. Weppner, *J. Solid State Chem.*, 2001, **158**, 279; (*b*) V. Thangadurai and W. Weppner, *Chem. Mater.*, 2002, **14**, 1136; (*c*) Y. Kobayashi, J. A. Schottenfeld, D. D. Macdonald and T. E. Mallouk, *J. Phys. Chem. C*, 2007, **111**, 3185.

4 (*a*) K. Toda, T. Teranishi and M. Sato, *J. Eur. Ceram. Soc.*, 1999, **19**, 1925; (*b*) M. Kato, Y. Imai, T. Kajita, Y. Takarabe, T. Minakawa, K. Nemoto, H. Tezuka, T. Nojia and Y. Koike, *Mater. Sci. Eng., B*, 2008, **148**, 53.

5 M. Fang, C.-H. Kim and T. E. Mallouk, *Chem. Mater.*, 1999, **11**, 1519.

6 (*a*) S. Ida, C. Ogata, M. Eguchi, W. J. Youngblood, T. E. Mallouk and Y. Matsumoto, *J. Am. Chem. Soc.*, 2008, **130**, 7052; (*b*) J. Y. Kim, H. Hiramatsu and F. E. Osterloh, *J. Am. Chem. Soc.*, 2005, **127**, 15556.

7 (*a*) K. Domen, J. Yoshimura, T. Sekine, A. Tanaka and T. Onishi, *Catal. Lett.*, 1990, **4**, 339; (*b*) K. Domen, Y. Ebina, T. Sekine, A. Tanaka, J. Kondo and C. Hirosei, *Catal. Today*, 1993, **14**, 479.

8 J. Yoshimura, Y. Ebina, J. Kondo, K. Domen and A. Tanaka, *J. Phys. Chem.*, 1993, **97**, 1970.

9 Y. Ebina, A. Tanaka, J. N. Kondo and K. Domen, *Chem. Mater.*, 1996, **8**, 2534.

10 (*a*) Y. Ebina, T. Sasaki, M. Harada and M. Watanabe, *Chem. Mater.*, 2002, **14**, 4390; (*b*) Y. Ebina, N. Sakai and T. Sasaki, *J. Phys. Chem. B*, 2005, **109**, 17212.

11 (*a*) M. Machida, J. Yabunaka, T. Kijima, S. Matsushima and M. Arai, *Int. J. Inorg. Mater.*, 2001, **3**, 545; (*b*) M. Machida, T. Mitsuyama, K. Ikeue, S. Matsushima and N. Arai, *J. Phys. Chem. B*, 2005, **109**, 7801; (*c*) T. Mitsuyama, A. Tsutsumi, T. Hata, K. Ikeue and M. Machida, *Bull. Chem. Soc. Jpn.*, 2008, **81**, 401.

12 (*a*) O. C. Compton, E. C. Carroll, J. Y. Kim, D. S. Larsen and F. E. Osterloh, *J. Phys. Chem. C*, 2007, **111**, 14589; (*b*) O. C. Compton, C. H. Mullet, S. Chiang and F. E. Osterloh, *J. Phys. Chem. C*, 2008, **112**, 6202.

13 H. Hata, Y. Kobayashi, V. Bojan, W. J. Youngblood and T. E. Mallouk, *Nano Lett.*, 2008, **8**, 794.

14 K. Izawa, T. Yamada, U. Unal, S. Ida, O. Altuntasoglu, M. Koinuma and Y. Matsumoto, *J. Phys. Chem. B*, 2006, **110**, 4645.

15 H. Fukuoka, T. Isami and S. Yamanaka, *J. Solid State Chem.*, 2000, **151**, 40.

16 K. Maeda, M. Eguchi, W. J. Youngblood and T. E. Mallouk, *Chem. Mater.*, 2008, **20**, 6770.

17 K. Maeda and K. Domen, *J. Phys. Chem. C*, 2007, **111**, 7851.

18 B. Kraeutler and A. J. Bard, *J. Am. Chem. Soc.*, 1978, **100**, 4317.

19 A. Takagaki, M. Sugisawa, D. Lu, J. N. Kondo, M. Hara, K. Domen and S. Hayashi, *J. Am. Chem. Soc.*, 2003, **125**, 5479.

20 (*a*) J.-M. Jehng and I. E. Wachs, *Chem. Mater.*, 1991, **3**, 100; (*b*) S.-H. Byeon and H.-J. Nam, *Chem. Mater.*, 2000, **12**, 1771.

21 R. D. Shannon, *Acta Crystallogr., Sect. A: Cryst. Phys., Diffr., Theor. Gen. Cryst.*, 1976, **32**, 751.

22 N. F. Mott and E. A. Davis, *Electronic Processes in Non-Crystalline Materials*, Oxford Univ. Press, Oxford, 2nd edn, 1979, pp. 272–306.

23 The band-gap energies were larger than the apparent band-gap energies when direct transition is assumed for light absorption by the samples. On the other hand, the assumption of indirect transition is in good agreement with apparent band-gap energies, suggesting that the present nanosheet materials are indirect band-gap semiconductors.

24 Y. Miseki, H. Kato and A. Kudo, *Energy Environ. Sci.*, 2009, **2**, 306.

25 (*a*) M. Wiegel, M. H. J. Emond, E. R. Stobbe and G. Blasse, *J. Phys. Chem. Solids*, 1994, **55**, 773; (*b*) G. Blasse and L. G. J. de Haart, *Mater. Chem. Phys.*, 1986, **14**, 481.

26 Y. Matsumoto, *J. Solid State Chem.*, 1996, **126**, 227.

27 J. F. Reber and K. Meier, *J. Phys. Chem.*, 1986, **90**, 824.

28 H. C. Youn, S. Baral and J. H. Fendler, *J. Phys. Chem.*, 1988, **92**, 6320.

29 I. Tsuji, H. Kato, H. Kobayashi and A. Kudo, *J. Am. Chem. Soc.*, 2004, **126**, 13406.

30 A. Kudo and I. Mikami, *J. Chem. Soc., Faraday Trans.*, 1998, **94**, 2929.

31 (*a*) H. Kato and A. Kudo, *Chem. Lett.*, 1999, 1207; (*b*) H. Kato and A. Kudo, *J. Phys. Chem. B*, 2001, **105**, 4285.

